Effects of Process Parameters on Friability and Surface Quality in the Rapid Investment Casting Process

Konstantin Fedorov[1], Comondore Ravindran[2], Kazem Fayazbakhsh[1]*
[1]Department of Aerospace Engineering, Toronto Metropolitan University, Toronto, Ontario M5B2K3, Canada
[2]Mechanical and Industrial Engineering, Toronto Metropolitan University, Toronto, Ontario M5B2K3, Canada
*Corresponding author: kazem@torontomu.ca; Tel: (+1) 416-979-5000 ext. 556414; fax: (+1) 416-979-5056;
https://orcid.org/0000-0003-3963-8282

Abstract

This research investigates surface erosion of ceramic shells in the Rapid Investment Casting (RIC) process using a friability test and microscopy analysis. The impact of different pattern materials, shell facecoat composition, and burnout temperature are explored. Acrylonitrile Butadiene Styrene (ABS), Polylactic Acid (PLA), and Polyvinyl Butyral (PVB) feedstock are used to make patterns by 3D printing, while a fourth benchmark set is produced from foundry wax in a rubber mold. The patterns are made in a cylindrical shape and invested in silica-based ceramic shells. The facecoat composition is varied by the addition or the absence of stucco in the primary slurry coat. The shells are burned out at temperatures of 700, 900, and 1100 °C, and used for a friability test. Additionally, a set of smaller shell samples is made for microscopic analysis of shell erosion at the pattern-ceramic interface. Results show that among 3D printing feedstock, ABS produces the most surface erosion as revealed by friability measurements and micrographs, while PVB is the least and is comparable to conventional foundry wax. The absence of stucco in the facecoat reduces friability by 25%, 35%, 55%, and 80% for ABS, PLA, PVB, and wax, respectively. Burnout temperature has a varying effect on friability depending on the pattern material. A strong link between the surface quality of castings and friability is found.

Keywords

Friability, Fused Filament Fabrication, Polyvinyl Butyral, Rapid Investment Casting, Stucco Penetration, Surface Tension.

Abbreviations

ABS Acrylonitrile Butadiene Styrene
DMA Dynamic Mechanical Analysis
FFF Fused Filament Fabrication
IC Investment Casting
PLA Polylactic Acid
PVB Polyvinyl Butyral
RIC Rapid Investment Casting
SEM Scanning Electron Microscopy
SLA Stereolithography Apparatus
SLS Selective Laser Sintering

1. Introduction.

The Rapid Investment Casting (RIC, Fig. 1) process differs from traditional Investment Casting (IC) in the use of additive manufacturing technologies to produce sacrificial patterns [1]. The time and cost savings offered by RIC makes it attractive for low-volume production and complex patterns difficult to produce by injection molding, such as shapes generated by topology optimization [2]. The method offers flexibility to create complex patterns directly from a CAD file and avoids the requisite tooling stage used in the conventional process [2, 3]. Wax-based patterns in traditional IC are prone to shrinkage in thicker sections and distortion of slender features when the pattern is removed from the injection-molding die [4]. However, RIC gives the ability to make thin-walled geometries with close control of dimensional tolerances due to the rigidity of 3D-printed patterns. Most importantly, RIC offers a much lower capital expense compared to direct metal 3D printing technologies such as Selective Laser Sintering (SLS).
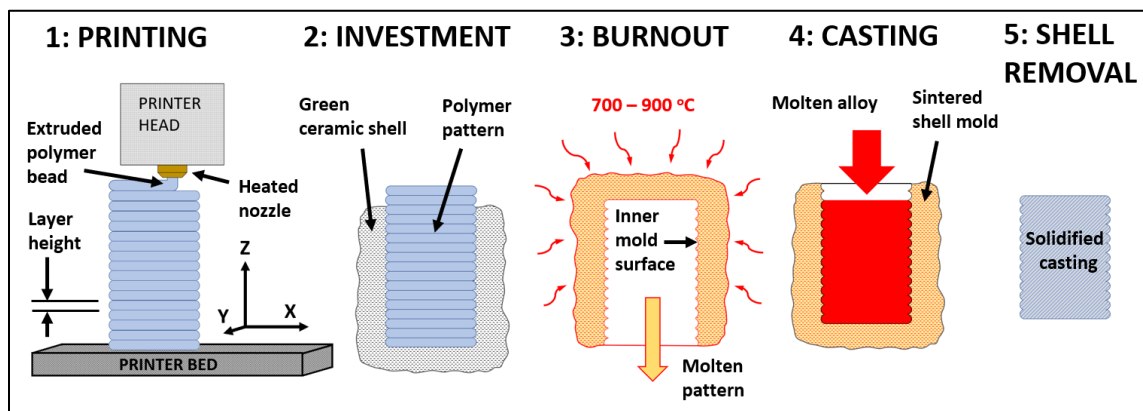

Fig. 1. Rapid Investment Casting process: (1) 3D printing of the pattern; (2) shell building process with ceramic shell slurry and stucco; (3) pattern burnout and shell sintering; (4) casting of the alloy; (5) shell removal.

The advantages of RIC over traditional IC are offset by the challenges associated with 3D printing, such as mold cracking, extra roughness introduced by stair-stepping, and additional ash remaining after burnout [5-9]. Most 3D printing feedstock used in the Fused Filament Fabrication (FFF) and Stereolithography Apparatus (SLA) processes have higher melting points than paraffin-based foundry wax, typically well above 200 °C as compared to 60 °C for IC wax. Because of this, the 3D-printed patterns tend to produce distortion and cracking of shells during burnout due to thermal expansion, with the resulting loss of geometrical tolerances [7, 8]. Paraffin wax is not as prone to thermal expansion issues because it will first melt as a thin layer on the pattern surface and quickly drain out or become absorbed into the shell porosity. This will occur before the bulk of a pattern mass can expand and crack the shell [4]. Steam autoclaving is often used for shell dewaxing in IC, providing a clean and rapid removal of wax that can be recycled afterward [4]. This is not possible for 3D-printed polymer patterns as the steam autoclave temperatures are not high enough to melt them out completely; hence traditional burnout is required for RIC. Stair-stepping surface roughness is another issue in RIC, which can be mitigated by making the pattern with thinner print layers [7-9] and by smoothing the pattern surface with solvent or sealer. Additionally, RIC patterns can produce ash residues after burnout that can react with the molten alloy and create surface pitting on a casting.

Ash residues from the wax patterns are a well-known issue in the IC industry, which to some extent, may be explained by a mechanism where ceramic shell particles are eroded from the inner mold surface during burnout. Post-burnout residue in the shell is often attributed to ash that originated from pyrolyzed wax. Little research has been done in analyzing the composition of these residues, but they are directly associated with a decrease in surface quality, as evidenced by surface roughness and pitting on castings [4, 9]. Studies on a jewelry RIC process [9] that used 3D-printed thermoset patterns made a link between the ash residues and erosion of the inner mold surface during burnout. Interactions between the 3D-printed pattern and the mold during burnout can cause breakage of weakly-bonded particles from the mold surface. The loose particles will remain in the shell as fine powder and can often be mistaken for ash. These "ash" particles scattered on the mold surface may cause pitting on the finished casting. Some of these loose particles can become incorporated into the flowing metal, forming inclusions in the solidified casting that may create stress concentrations later in service [10].

A friability test for ceramic shells has been described in prior research to measure the degree of shell erosion and the presence of loose mold fragments [11, 12]. The process involves investing a cylindrical wax rod in a ceramic shell, then burning out the pattern and sintering at a controlled temperature. The resulting shell is weighted on a microbalance, scraped with a brush, and weighed again to measure the loss of mass. Friability in the case of ceramic shells is a measure of the loss of ceramic mass per unit of surface area. It is an indicator that portends potential inclusion and roughness defects in the final casting and should be minimized by adjusting process parameters. Prior literature has mainly focused on the impact of polymer additives in the primary slurry and sintering temperature on the shell friability [11, 12]. The composition and physical characteristics of the primary slurry directly affect the green strength of the facecoat during burnout and its friability after sintering. Some of these characteristics may be the slurry viscosity, stucco particle morphology and size distribution, and concentration of various slurry additives. Additionally, drying techniques and humidity levels will influence the microstructure and strength of the facecoat, whose effect can be measured with a friability test.

Process parameters such as the shell sintering temperature have been explored for their impact on shell friability in conventional IC [11, 12]. It was shown that higher sintering temperatures lead to a decrease in friability. This is primarily due to a greater degree of shell vitrification, where loosely held particles become less susceptible to abrasion by the test brush. The bulk of the facecoat layer consists of a dry stucco material that is applied to the pattern after dipping into the primary slurry. The facecoat stucco particle size distribution and morphology are known to impact cast surface quality in conventional IC [4]. Casting roughness due to stucco application on the facecoat is known as stucco penetration in IC [4]. The cause of stucco penetration has been explained by the entrapment of air pockets onto the pattern surface by primary stucco due to large stucco particle size, high application velocity, and low slurry viscosity [4]. The resulting casting may have roughness issues. For this reason, the general foundry practice is to apply smaller stucco grit sizes to the facecoat and larger grits in the backup coats. The impacts of shell sintering temperature and composition of the facecoat are therefore of primary interest in the present RIC study.

Prior research in RIC that focused on cast surface roughness [5, 8, 9, 13, 14] utilized the FFF process to make ABS patterns that were invested and cast in various alloys. ABS appears to be the most widely used feedstock made by FFF and has become an established precedent in RIC research [7]. Other materials, such as Polylactic Acid (PLA) and Polyvinyl Butyral (PVB) [3], have also been explored, with PVB appearing to be the most promising due to its low ash content. PolyCast™ is a PVB-based feedstock that was specially

developed for RIC by Polymaker. It is reported to exert minimal thermal expansion stress on the ceramic shell molds [3, 7] and is advertised to have an ash content of 0.003% [6], which is lower than the paraffin wax used in the current experiment.

To the authors' knowledge, there have been no reports on friability analysis in RIC as a product of pattern material properties together with facecoat composition and burnout temperature. Because casting surface issues such as roughness and pitting are more common in RIC literature [9, 13, 14] than in IC, friability should be used as a metric for evaluating the severity of these defects. Their root cause may originate from differences in the thermophysical properties of RIC materials to those of IC wax. Hence, it is of interest to compare how shell friability varies among different pattern materials, with paraffin wax serving as the IC industry benchmark material.

For the present research, pattern material, facecoat composition, and burnout temperature were selected as process parameters that may influence ceramic shell friability. Three 3D printing polymers, two facecoat compositions, and three burnout temperatures are explored. Section 2 describes the pattern design and 3D printing process followed by the investment and burnout procedures. Then, the friability measurements and micrograph analysis are explained. Results are presented in Section 3, followed by discussion, conclusions, and recommendations for future research.

2. Methodology

The complete sample set for all patterns was made in two batches, one where 50/100-grit stucco was applied to the facecoat and a second batch without any facecoat stucco. The effects of pattern material properties were assessed by using three 3D-printed thermoplastics (Acrylonitrile Butadiene Styrene: ABS, Polylactic Acid: PLA, and Polyvinyl Butyral: PVB) and IC wax, whose thermophysical properties are listed in Table 1. The ABS, PLA, and PVB patterns were 3D-printed with the FFF technique, and the foundry wax patterns were cast in a mold. The melting points of these materials vary from high to low in the respective order and were anticipated to have a related effect on friability. The last process parameter was burnout temperature, which may affect the rate at which the outer pattern surface melts and gets absorbed by the shell porosity. Burnout at higher temperatures was anticipated to produce more shell erosion and friability due to intense ebullition and vapor pressure exerted on inner shell surfaces by the evaporating pattern, described by Beeley [4].

Table 1. Mechanical and thermal properties of pattern materials.

Physical Property	ABS – 3D Printing Canada - Natural	PLA – NatureWorks Ingeo^{TM} Biopolymer 4043d	PVB – ColorFab PolyCast^{TM}	Ferris® 2194 Injection Wax
Density	1.03 g/cm^3	1.24 g/cm^3	1.1 g/cm^3	0.96 g/cm^3
$T_{Glass\ Transition}$	97 °C	55-60 °C	70 °C	60 °C
$T_{Melting}$	220-240 °C	145-160 °C	130-160 °C	67 °C
Young's Modulus	2030 MPa	3600 MPa	1594-1896 MPa	200 MPa
Yield Strength	43.6 MPa	60 MPa	34-37.4 MPa	0.9 MPa
Ash Content	n/a	n/a	0.003%	0.006%

2.1. Pattern description and manufacturing

The friability samples were prepared by 3D printing two sets of cylindrical patterns from ABS, PLA, and PVB feedstock on the Anycubic Chiron FFF 3D printer. The cylinders had a diameter of 25 mm and length of 150 mm (Fig. 2). The 3D printing parameters common to the three materials are as follows: layer thickness of 0.1 mm, nozzle diameter of 0.4 mm, extrudate width of 0.4 mm, grid-type infill of 15%, and a wall thickness of 1.5mm. The remaining parameters are summarized in Table 2. The cylinders were printed in the up-right direction, ZXY per ISO/ASTM 52921:2013(E). The wax specimens (two sets) were made by vacuum casting in a rubber mold. The mold was made in a castable two-part polyurethane rubber that was molded from an ABS 3D-printed sample, duplicating its geometry and surface texture.

Fig. 2. Materials for friability measurement: 3D-printed ABS pattern, ceramic shell after burnout (700 °C), and test brush.

Table 2. 3D printing parameters for ABS, PLA, and PVB patterns.

Material	Design/Manufacturing Parameter	Value	Design/Manufacturing Parameter	Value
ABS	Bed temperature	100 °C	Nozzle temperature	215 °C
	Printing speed	40 mm/sec	Cooling	No fan cooling
PLA	Bed temperature	60 °C	Nozzle temperature	205 °C
	Printing speed	50 mm/sec	Cooling	Yes
PVB	Bed temperature	60 °C	Nozzle temperature	200 °C
	Printing speed	50 mm/sec	Cooling	Yes

ABS was chosen in the study as it was used for RIC patterns in prior research due to good dimensional stability in 3D printing. It is therefore of interest to show how ABS will compare to PLA, PVB, and wax. PLA was selected as the material of choice in the 3D printing community for its ease of printing in contrast to other feedstock, which may suffer from defects such as delamination and warpage. PVB was also chosen because it was specifically made by one manufacturer, Polymaker, for RIC and is advertised to have a low ash content of 0.003% [6] while having the same 3D printing characteristics as PLA. The paraffin wax patterns were made to serve as IC industry-standard benchmark material.

For the first set of shells with facecoat stucco, four cylinders were made in each material (ABS, PLA, PVB, wax) for three burnout temperatures (700, 900, and 1100 °C), a total of twelve samples. The second set was made in a like manner but without stucco in the facecoat. In total, twenty-four cylindrical samples were prepared for the friability tests (Fig. 2 shows an example for ABS only). Additionally, smaller specimens were made for micrograph analysis of the shells (Fig. 3). These were printed in rectangles of 20 x 60 x 3 mm. The patterns were invested in a ceramic shell and burned out at 700 °C. The shell surfaces were first imaged with optical and Scanning Electron Microscopy (SEM) microscope, then set in epoxy resin, sectioned, and polished for SEM micrography. The cross-section micrographs were used to examine the microstructure of the inner shell surface. Small wax specimens were likewise made with a rubber mold, as was done for cylinders.
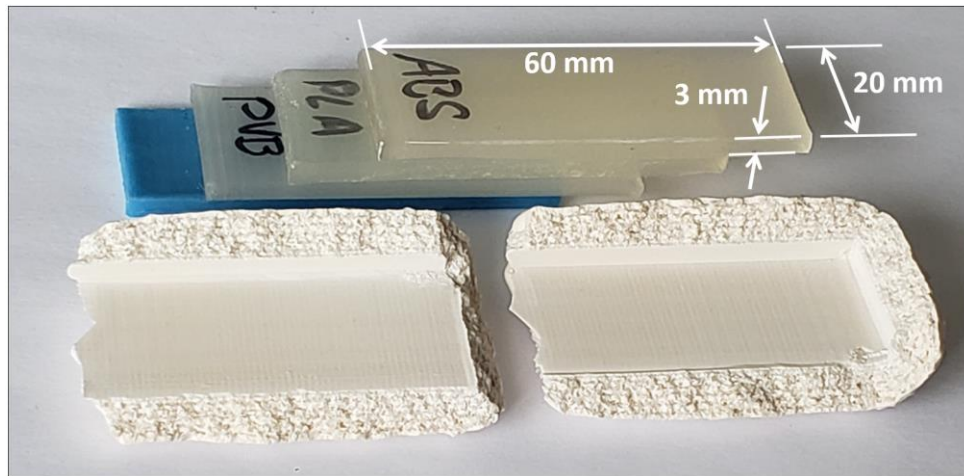

Fig. 3. Patterns and shells for micrography analysis: (top) ABS, PLA, PVB, and wax patterns prior to investment; (bottom) a sample of a split ceramic shell from a PVB pattern after burnout, 700 °C.

2.2. Investment and burnout

The ceramic shell slurry was a premixed product based on colloidal silica and fused silica flour (SuspendaSlurry® by Ransom & Randolph), which is made with an additive allowing the silica flour to stay suspended without continuous mixing. The slurry had a viscosity reading of 20 seconds, measured by a no. 5 Zahn cup. The composition of all shell layers is summarized in Table 3. The first set of cylinder patterns was dipped in the slurry for 5 seconds and allowed to drain for 30 seconds while the pattern was manually rotated for a uniform slurry coat. Fused silica powder (Ransom & Randolph) was applied manually from a height of 20 cm. Drying took place with natural air currents at 20 °C and 60% relative humidity and 12hrs between layers. The second set of cylinders without stucco in the facecoat were dipped for 5 seconds, followed by a 5-minute drainage period while the pattern was rotated. This facecoat was allowed to dry without the application of stucco. After completion, the shell cylinder ends were cut off with a diamond saw (Fig. 2). Ceramic shells for SEM micrographs were prepared likewise.

Table 3. Ceramic shell composition for the two facecoat types.

Layer	Samples with facecoat stucco	Samples without facecoat stucco
Facecoat	Slurry + 50/100 mesh silica stucco	Slurry without stucco

2nd layer	Slurry + 30/50 mesh silica stucco	Slurry + 50/100 mesh silica stucco
3rd – 6th layers	Slurry + 30/50 mesh silica stucco	Slurry + 30/50 mesh silica stucco
Last sealing layer	Slurry without stucco	Slurry without stucco

All friability samples were burned out and sintered at temperatures of 700, 900, and 1100 °C (± 10 °C) for one hour in an electric resistance furnace. Prior to burnout, the furnace was preheated to the required temperature, and each sample inserted for a one-hour burnout and sintering cycle. The furnace was equipped with a 20 x 50 mm vent, that was left open for the cycle duration.

2.3. Measurement of friability and micrographs

Friability is a measure of the mold mass lost per unit area after a brush passes through the ceramic shell cylinder and is given by the equation:

$$F = G/\pi DL \tag{1}$$

Where D is the internal diameter, L is the sample length, and G is the measured mass change. The cylinders were weighed on a microbalance (Scientech, SP350) with a +/- 0.001 g precision, brushed (plastic bristle brush, 30mm diameter x 60mm long), blown out with compressed air at 5 psi, and weighed again. Each sample's dimensions and the mass loss provided friability values in kg/m^2. The smaller shell specimens were split open to expose the inner surface for microscopic examination. Micrographic samples of these specimens were prepared by sectioning and mounting them in epoxy resin, followed by successive grinding and polishing down to 0.1-micron grit (aluminum oxide). The small shells and micrograph samples were examined using an optical microscope and an SEM (JEOL, model JSM6380LV).

3. Results

3.1. Friability measurements

Friability measurements are shown in Fig. 4 for all material samples. ABS had the highest friability for all conditions, followed by PLA, PVB, and wax. Friability values in all samples containing no stucco in the facecoat were lower than those with stucco. ABS patterns without facecoat stucco have 25% lower friability than those with stucco, while PLA, PVB, and wax have a 35%, 55%, and 80% friability decrease, respectively.
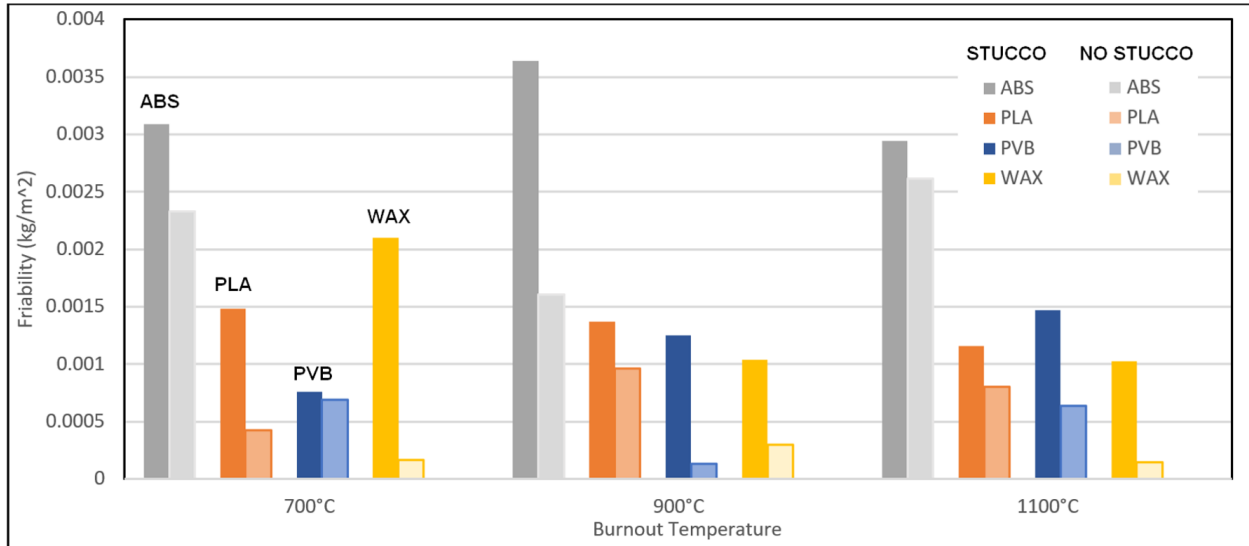
Fig. 4. The friability of ceramic shells prepared from ABS, PLA, PVB, and wax patterns, three different burnout temperatures, and two facecoat types (with and without stucco).

3.2 Visual examination of shell surfaces

Comparisons of shell surfaces for 700 °C burnout temperature are shown in Fig. 5. The shells reveal impressions of the print lines left on the ceramic shell from the 3D-printed patterns. Surfaces containing stucco in the facecoat (left side) have more surface pitting than facecoats containing no stucco (right side). The magnitude of this effect appears to agree with the surface damage as measured by friability (Fig. 4).
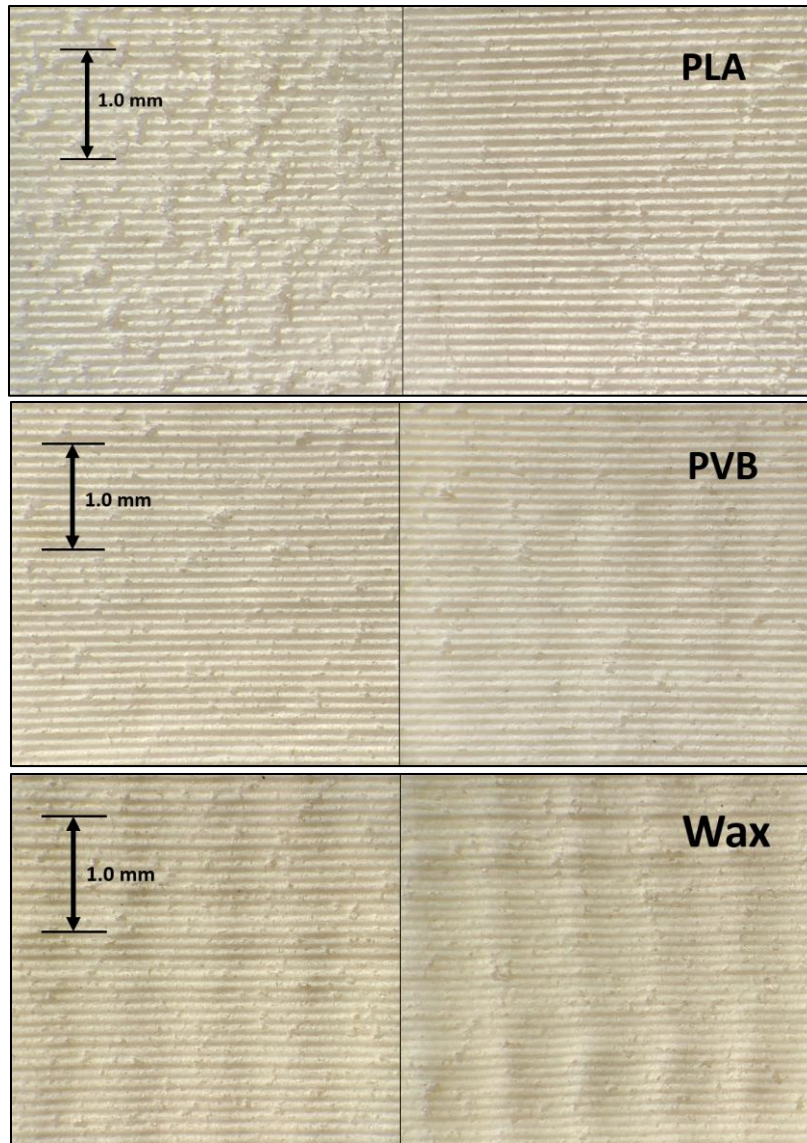
Fig.5. Ceramic shell surfaces prepared from different patterns after cleaning of shell debris, 700 °C burnout: (left) facecoat with stucco; (right) facecoat without stucco.

In both friability and micrograph samples, significant shell debris was found in the ABS and PLA ceramic shell samples. Fig. 6 shows this debris on an ABS-derived shell prepared for a micrograph. The debris was substantially less for PVB and wax shell samples. Visual assessment of shell surfaces revealed that PVB patterns behaved similarly to wax in terms of surface erosion and debris.
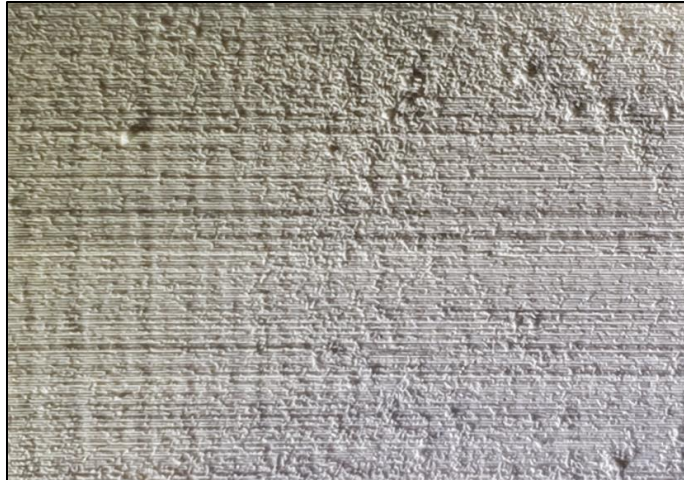
Fig.6. Ceramic shell debris on the interior shell surface: ABS micrograph pattern, 700 °C burnout.

3.3 SEM Micrography

Micrographs of a PVB-derived ceramic shell with a stucco-containing facecoat are shown in Fig. 7 and 8. Fig. 7 shows the post-burnout shell-pattern interface with the impressions of 3D print-line grooves of the PVB pattern. The facecoat fine slurry flour particles that were first in contact with the pattern are shown, followed by 50/100 grit primary stucco particles. Behind these are the larger 30/50 grit backup stucco particles in the second shell layer. Large voids can be seen between the primary stucco particles introduced during the stucco application.

Fig. 8 shows a closeup of the primary stucco particles in the same PVB sample. The structure of the ceramic shell matrix can be seen as consisting of the large silica stucco particles, the finer silica flour particles from the slurry, and the silica gel binder. The silica flour forms the bulk of the slurry mass and acts as a filler between the stucco particles, minimizing shrinkage during drying. The slurry colloidal silica binder that holds the whole shell matrix together appears in grey color in the micrograph. Aside from the voids between stucco particles, the same micrograph shows shrinkage cracks in the silica flour and binder (Fig. 8 (c)). The shrinkage cracks appear more prominently around the largest stucco particles.
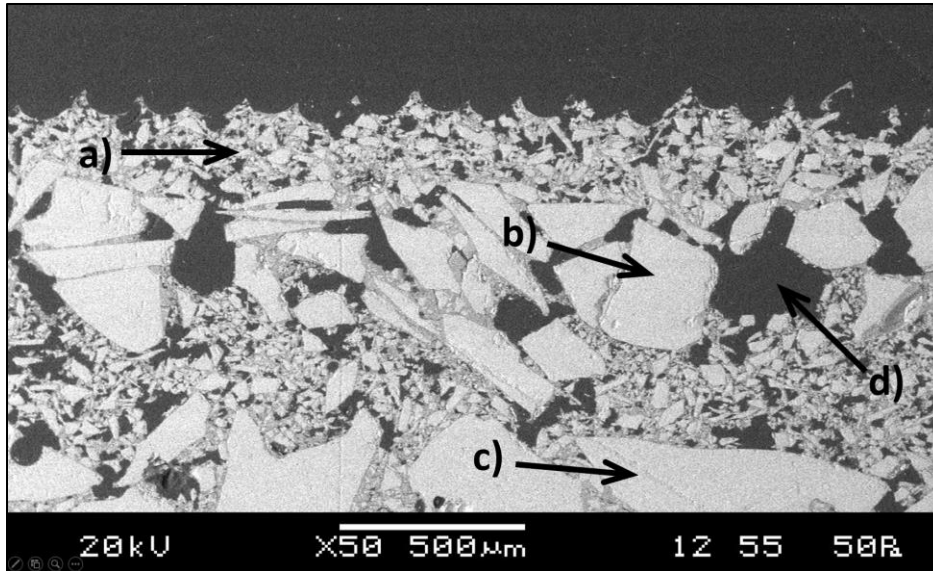
Fig. 7. SEM micrograph of a shell specimen with primary stucco applied to the facecoat, PVB pattern, 700 °C burnout: (a) facecoat slurry, silica flour; (b) facecoat primary stucco, fused silica 50/100 grit; (c) 2nd coat backup stucco, fused silica 30/50 grit; (d) voids introduced by the application of facecoat stucco.
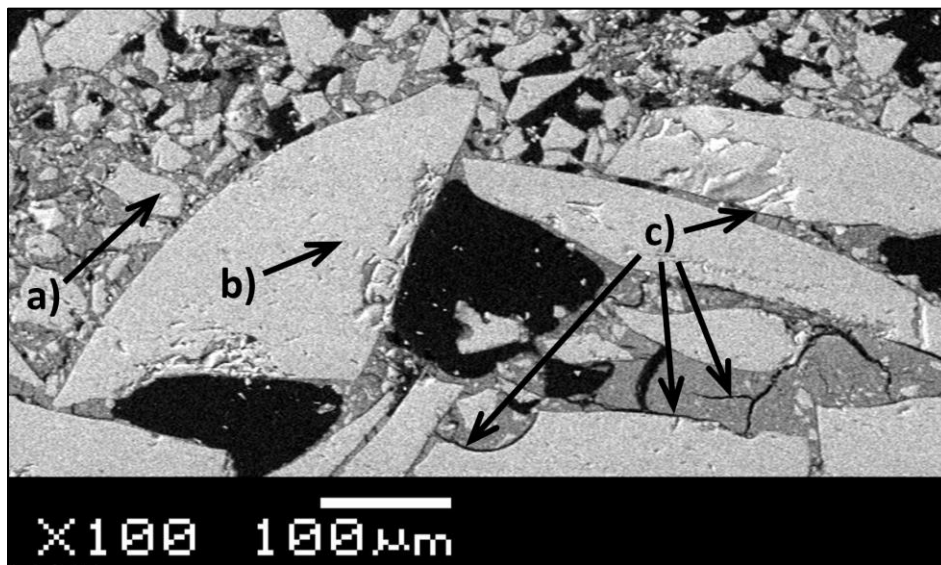

Fig. 8. SEM micrograph closeup of primary stucco particles, PVB pattern, 700 °C burnout: (a) silica flour particles from the shell slurry; (b) primary stucco particles; (c) shrinkage cracks from drying of the colloidal silica gel binder.

4. Discussion

Overall, the optical and SEM shell images reveal that the observed surface damage is in agreement with the friability chart in Fig. 4. Photographs of ABS-derived shell samples show the most surface pitting, which is also supported by the highest friability measurements for both types of facecoats in the ABS samples. Most of the loss of mass measured by friability likely originates from the loose or weakly bonded ceramic fragments dislodged during burnout from the shell surface (see Fig. 6 for ABS example). The friability of

shells ranged from 3.5 g to less than 1 g per square meter of shell area, which is at the low end of friability measurements reported in previous research [11, 12]. It should be noted that friability is a comparative measurement that can vary depending on the brush stiffness and size relative to the shell cylinder. Friability values are, therefore, comparable only for a single combination of brush type and cylinder diameter.

The increase of friability for samples with facecoat stucco could be explained by the micrographs in Fig. 7 & 8. The larger stucco particles are surrounded by voids and cracks that weaken the shell matrix. The application of stucco causes voids, while the cracks are caused by the drying shrinkage of the slurry and poor adhesion to the smooth surface of the stucco particles. Similar cracks surrounding stucco particles can be seen in micrographs of prior works [15, 16]. Because the fused-silica stucco particles have a smooth glass-like surface, the drying silica flour slurry can de-bond from the stucco due to shrinkage. The resulting cracks are especially evident around the largest particles, which tend to cause the most significant shrinkage of the slurry flour relative to stucco. Facecoat stucco particles that fell closest to the pattern surface during stucco application bring the voids and cracks closer to the pattern. This allows for more shell fracturing to take place during burnout due to interactions with the evaporating pattern. A thicker layer of silica flour on the pattern surface (Fig. 7 (a)) acts as a barrier that places these voids and cracks farther from the evaporating pattern. Samples without stucco in the facecoat had a thicker protective layer of silica flour without the voids and cracks mentioned above, resulting in less surface erosion during burnout. Higher sintering temperatures were reported to reduce friability in past publications [11, 12] because they tend to fuse more of the loosely held shell fragments. The results in the present study do not show a significant relationship between temperature and friability over the temperature range examined.

SEM surface images in Fig. 9 show the shells in the pre-burnout and post-burnout stages for ABS samples. An additional sample was prepared to analyze the pre-burnout shell surface by building a shell on one side of a thin-walled sheet of 3D-printed ABS. The ABS sheet was then dissolved from the shell in methyl ethyl ketone solvent, revealing the surface shown in Fig. 9 (a). The two post-burnout surface images, Fig. 9 (b) & (c), are taken from the same samples shown in Fig. 5 for ABS. Comparing the three surfaces in Fig. 9, the pre-burnout shell has some minor cracking due to the drying of the slurry. In contrast, post-burnout shells have more severe surface breakage due to interactions with the melting pattern mentioned earlier. The mechanism for shell erosion may be explained by the voids and cracks in the facecoat that absorb molten pattern material. When the pattern begins to expand and melt during burnout, some of it will be forced into these voids [4] and cracks by the thermal expansion pressure. As the temperature increases further, the vapor pressure from the evaporating pattern trapped in the shell may cause the weaker fragments of the shell to flake off. The greater degree of shell breakage from ABS and PLA patterns in contrast to PVB and wax may be due to the higher thermal expansion pressure exerted by these materials. In previous experiments conducted by the authors [7], ABS caused the largest shell distortion due to thermal expansion, followed by PLA and PVB in decreasing order. Hence, the higher thermal expansions of ABS and PLA could also contribute to increased friability.
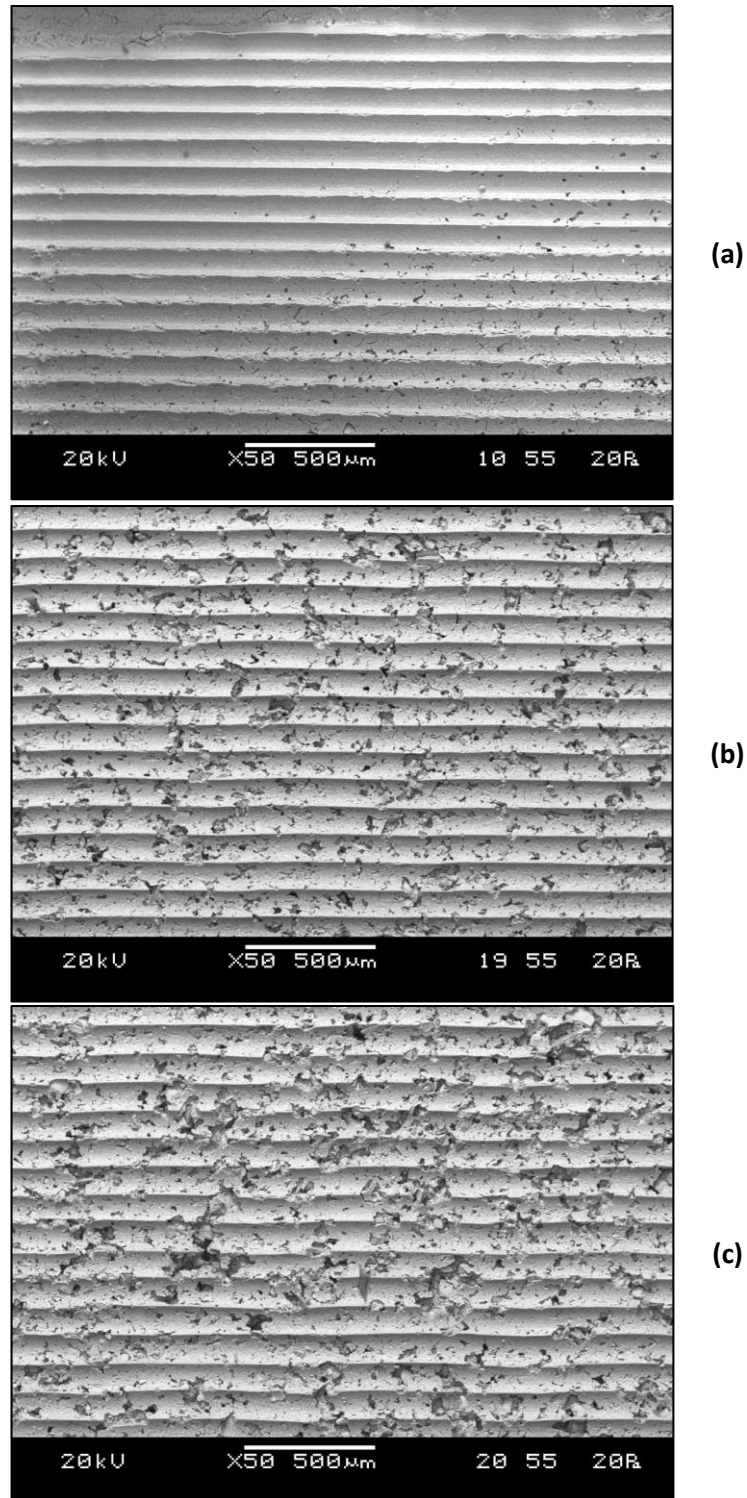
Fig. 9. SEM images of shell surfaces prepared with ABS patterns: (a) pre-burnout shell surface after the pattern was dissolved in a solvent; (b) 700 °C post-burnout shell surface without stucco; (c) 700 °C post-burnout shell surface with stucco. The larger silica flour and stucco particles are exposed to the surface in fragmented areas on the post-burnout samples (b) and (c).

From the shell micrograph and friability results, it can be concluded that PVB is a superior pattern material to ABS and PLA, in terms of cast surface roughness and potential inclusions. PVB is also a material of choice, as explored in prior research [3, 7], where it was found to produce no cracking of the shell due to thermal expansion forces, in contrast to pattern materials such as thermosetting resins, ABS, or PLA. Existing research on the thermomechanical properties of ABS, PLA, and PVB shows significant differences in the viscoelastic properties of these materials in a temperature range from 0 to 150 °C [17-19]. In Dynamic Mechanical Analysis (DMA), the loss modulus of a viscoelastic polymer measures the energy loss in deformation, which can be compared to the storage modulus that measures energy retention [20]. The ratio of the loss modulus to storage modus is the tan(δ), which can be plotted against temperature. Higher values of tan(δ) correspond to more fluid-like qualities of the polymer, which allow it to flow under pressure. DMA analysis in prior polymer research shows that tan(δ) increases with temperature and peaks rapidly at a point where most of the elasticity is lost. ABS, PLA, and PVB have maximum tan(δ) values at around 115, 70, and 30 °C, respectively [17-19]. These values suggest that PVB becomes more fluid-like at lower temperatures than ABS and PLA, making its softening properties closest to foundry wax. IC foundry wax has a melting point of about 60 °C and a correspondingly lower peak tan(δ) temperature. The lower tan(δ) value of PVB may allow it to conform to the particle texture on the inner mold surface without causing localized stresses and fragmentation that is detected in friability measurements.

The significance of shell fragmentation is in the deterioration of cast surface quality and the potential for shell inclusions in the casting. Fig. 10 shows example surfaces of A319 aluminum alloy castings poured into ceramic shells made using ABS, PLA, and PVB patterns from a prior publication by the authors [7]. The patterns were prepared using the same 3D printing parameters as in the present paper. The small fragments breaking from the shell tend to scatter in random areas in the mold, as shown in Fig. 6. During casting, the molten alloy will flow around these fragments due to liquid surface tension, forming a pitted surface. Fig. 10 shows the ABS and PLA-derived castings with more surface pitting than PVB, supporting the present friability measurements. The cast surface from a PVB pattern shows the impression left by 3D printing lines on the shell, each 0.1 mm wide (Fig. 10 (c)). Surfaces on ABS and PLA-derived castings faintly reveal these printing lines, which are obscured by the more prominent pitting defects.
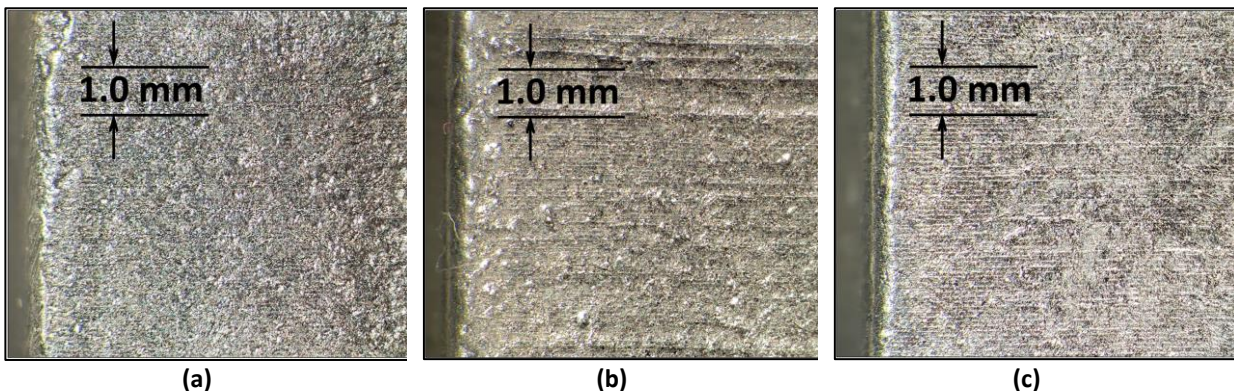

| (a) | (b) | (c) |

Fig. 10. Cast surfaces of A319 alloy, 700 °C burnout: (a) ABS pattern; (b) PLA pattern; (c) PVB pattern [7].

The formation of this pitting defect is illustrated in Fig. 11. Due to the non-wetting behavior of molten aluminum alloys on silica and alumina-based ceramics [7, 21, 22], the liquid surface makes a contact angle

θ with the ceramic (Fig. 11). In general, when the contact angle is above 90°, the surface is considered non-wetting. As described by Eustathopoulos et al. [21], the molten aluminum will take on a compound surface with two principal radii of curvature, R_1 and R_2, having a minimum surface tension energy summarized by the equation:

$$\rho g h = \sigma_{LV} \left(\frac{1}{R_1} + \frac{1}{R_2} \right) \qquad (2)$$

Where $\rho g h$ is the metallostatic pressure due to riser height, h, below the melt surface, and σ_{LV} is the liquid-vapor surface tension of the molten alloy. This equation applies to any point on the liquid surface not in contact with the ceramic. The two radii of curvature, R_1 and R_2, are on opposite sides of the liquid surface (Fig. 11) and will have opposite signs in Eq. 2. This will tend to decrease R_1 with a decrease in R_2. Higher metallostatic pressure $\rho g h$ will force the liquid metal closer to the fragment surface, resulting in smaller radii of curvature and a smaller pit diameter D_p. The bell-shaped liquid surface formed around a shell fragment will turn into a pit with a diameter D_p after solidification.
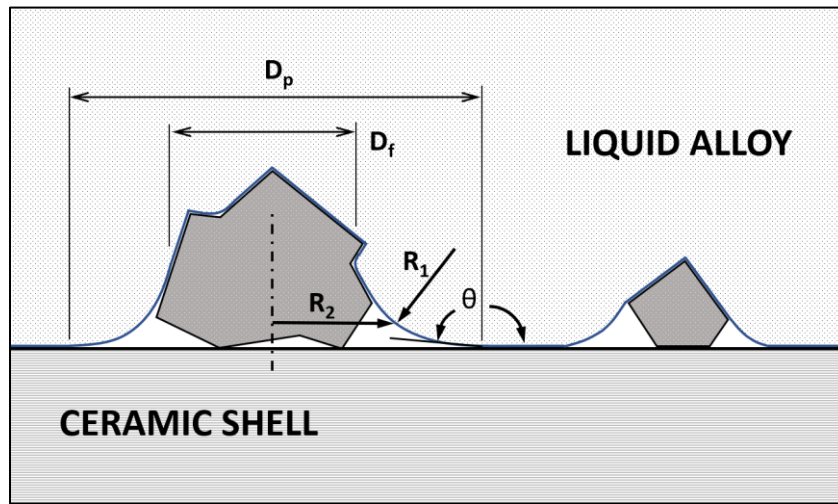

Fig. 11. Ceramic fragments in contact with liquid alloy. Shell fragments with an average diameter D_f will create a pit of a larger diameter D_p due to surface tension.

Reducing the size and concentration of large stucco particles near the pattern surface can alleviate the ceramic shell microfractures during drying and burnout. Control of the shell morphology near the pattern can reduce friability and the associated problems of casting roughness and inclusions. This can be done by using a finer stucco grit to reduce the size of surrounding voids and cracks or by decreasing the fall velocity of stucco during its application. As discussed earlier, it is already a standard practice in the IC industry to apply smaller stucco grit sizes in the facecoat to improve cast surface quality [4]. Stucco particles with a higher surface roughness may also enhance bonding with the facecoat silica flour/gel matrix. For this purpose, ceramic mullite grog could be tried due to the round particle shape with a rough surface.

5. Conclusions

The present research demonstrated that ceramic shell friability and the associated casting defects may be significantly reduced in FFF-based RIC by using PVB patterns as opposed to ABS and PLA. The separation distance between the larger stucco particles and the pattern surface substantially affects the friability of ceramic shell molds. Friability decreases by 25%, 35%, 55%, and 80% for ABS, PLA, PVB, and wax, respectively, when the facecoat does not contain stucco. The highest reduction of friability due to stucco was observed with wax patterns, signifying that the present research also applies to the conventional IC industry. Using PVB patterns in combination with a modified facecoat (no stucco) will produce the largest reduction of surface flaws such as roughness and pitting. Because ceramic shell inclusion defects are associated with friability, they can also be mitigated likewise. ABS and PLA patterns with stucco in the facecoat will produce the worst case in surface quality and shell inclusion defects. The methodology presented in this paper can also be applied to RIC methods that use other 3D printing technologies, such as SLA and Selective Laser Sintering (SLS).

Additional research may be conducted by exploring alternative facecoat stucco materials, such as mullite grogs with higher particle surface roughness and various particle size distributions. The mesh size and shape of primary stucco particles can affect the size of cracks resulting from drying shrinkage. Spherical stucco grains will have a lower surface-to-volume ratio, potentially decreasing the surface area of cracks. Stucco application velocity and drying conditions should also be explored for their effects on drying shrinkage and friability.

This research empirically shows that the shell composition and thermomechanical properties of the pattern significantly affect friability. However, the performed tests cannot explain the exact mechanisms taking place at a microscopic level on the shell-pattern interface during burnout. The pattern material properties considered in this study are for solid and semi-liquid states only. The available data for thermoplastic polymers is limited to narrow temperature ranges applicable for industrial uses and not for burnouts spanning from 20 to 1100 °C. Comprehensive thermomechanical and thermal analyses are needed from solid to liquid and vapor states for the temperature range encountered during burnout. Data for the polymer viscosity and thermal expansion as a function of temperature, boiling points, and specific heats will be required to formulate a more detailed model for interactions at the shell-pattern interface and their effects on friability.

References:

[1] Singh, Rupinder, and Gurwinder Singh. "Investigations for statistically controlled investment casting solution of FDM-based ABS replicas." *Rapid Prototyping Journal* (2014).

[2] Kang, Jin-wu, and Qiang-xian Ma. "The role and impact of 3D printing technologies in casting." *China Foundry* 14.3 (2017): 157-168.

[3] Körber, S., Völkl, R. and Glatzel, U., 2021. 3D printed polymer positive models for the investment casting of extremely thin-walled single crystals. Journal of Materials Processing Technology, 293, p.117095.

[4] Beeley, Peter R., and Robert F. Smart, eds. *Investment casting*. London: Institute of Materials, 1995.

[5] Singh, Jaspreet, Rupinder Singh, and Harwinder Singh. "Surface roughness prediction using Buckingham's Pi-theorem for SS-316L hip implant prepared as rapid investment casting." *Materials Today: Proceedings* 5.9 (2018): 18080-18088.

[6] Investment Casting with PolyCast™. Polymaker Application Note.

[7] Fedorov, K., Fayazbakhsh, K. and Ravindran, C., 2022. Surface roughness and dimensional tolerances in A319 alloy samples produced by rapid investment casting process based on fused filament fabrication. The International Journal of Advanced Manufacturing Technology, pp.1-15.

[8] Singh, Sunpreet, and Rupinder Singh. "Fused deposition modelling based rapid patterns for investment casting applications: a review." *Rapid Prototyping Journal* (2016).

[9] Binnion, J. and Arts, J.B.M., 2016. A New Method for Preparing 3D Acrylic Photopolymer Patterns for Investment Casting. In *Proceedings of the Santa Fe Symposium on Jewelry Manufacturing Technology*.

[10] Campbell, J., 2020. *The Mechanisms of Metallurgical Failure: On the Origin of Fracture*. Butterworth-Heinemann.

[11] Yuan, C., Compton, D., Cheng, X., Green, N. and Withey, P., 2012. The influence of polymer content and sintering temperature on yttria face-coat moulds for TiAl casting. Journal of the European Ceramic Society, 32(16), pp.4041-4049.

[12] Yuan, C., Cheng, X., Holt, G.S., Shevchenko, D. and Withey, P.A., 2015. Investment casting of Ti–46Al–8Nb–1B alloy using moulds with CaO-stabilized zirconia face coat at various mould pre-heat temperatures. Ceramics International, 41(3), pp.4129-4139.

[13] Chhabra, Munish, and Rupinder Singh. "Rapid casting solutions: a review." Rapid Prototyping Journal (2011).

[14] Cheah, Chi Mun, et al. "Rapid prototyping and tooling techniques: a review of applications for rapid investment casting." The International Journal of Advanced Manufacturing Technology 25.3 (2005): 308-320.

[15] Jones, S. and Yuan, C., 2003. Advances in shell moulding for investment casting. Journal of Materials Processing Technology, 135(2-3), pp.258-265.

[16] Xu, M. and Qing, J., 2019. Effect of firing temperature and duration on fused silica investment shell strength at room temperature. International Journal of Metalcasting, 13(4), pp.923-927.

[17] Song, P., Cao, Z., Meng, Q., Fu, S., Fang, Z., Wu, Q. and Ye, J., 2012. Effect of lignin incorporation and reactive compatibilization on the morphological, rheological, and mechanical properties of ABS resin. Journal of Macromolecular Science, Part B, 51(4), pp.720-735.

[18] Kamthai, S. and Magaraphan, R., 2015, May. Thermal and mechanical properties of polylactic acid (PLA) and bagasse carboxymethyl cellulose (CMCB) composite by adding isosorbide diesters. In AIP conference proceedings (Vol. 1664, No. 1, p. 060006). AIP Publishing LLC.

[19] Ramos, A., Pelayo, F., Lamela, M.J., Canteli, A.F., Huerta, M.C. and Pacios, A., 2013, April. Evaluation of damping properties of structural glass panes under impact loading. In Proceedings of COST Action TU0905 Mid-term Conference on Structural Glass, Taylor & Francis Group (pp. 113-120).

[20] Margolis, J.M., 2006. Engineering plastics handbook. McGraw-Hill Education.

[21] Eustathopoulos, N., Nicholas, M.G. and Drevet, B. eds., 1999. Wettability at high temperatures. Elsevier.

[22] Molina, J.M., Voytovych, R., Louis, E. and Eustathopoulos, N., 2007. The surface tension of liquid aluminium in high vacuum: the role of surface condition. International journal of adhesion and adhesives, 27(5), pp.394-401.

Statements & Declarations

Data availability statement

The raw/processed data required to reproduce these findings cannot be shared at this time as the data also forms part of an ongoing study.

Competing Interests

The authors have no relevant financial or non-financial interests to disclose.

Author Contributions

All authors contributed to the study conception and methodology. Konstantin Fedorov performed validation, formal analysis, and investigation. Konstantin Fedorov wrote the first draft of the manuscript, and all authors reviewed and provided comments on all versions of the manuscript. Comondore Ravindran and Kazem Fayazbakhsh supervised the research work, administered the project, and provided funding.